Nature Communications

https://doi.org/10.1038/s41467-026-70976-1

Article in Press

Engineering non-interfacial hydrogen spillover in a $Ni_{17}W_3$-WO_2 heterostructure

Received: 20 May 2025

Accepted: 9 March 2026

Cite this article as: Xie, S., Dong, H., Cao, S. *et al.* Engineering non-interfacial hydrogen spillover in a $Ni_{17}W_3$-WO_2 heterostructure. *Nat Commun* (2026). https://doi.org/10.1038/s41467-026-70976-1

Song Xie, Hao Dong, Shuang Cao, Yaping Miao, Liwei Xiong, Biao Gao, Xuming Zhang, Imran Shakir, Yongchao Yao, Xiang Peng & Xuping Sun

Engineering non-interfacial hydrogen spillover in a $Ni_{17}W_3$-WO_2 heterostructure

Song Xie[1], Hao Dong[1], Shuang Cao[1], Yaping Miao[2], Liwei Xiong[1], Biao Gao[3], Xuming Zhang[3], Imran Shakir[4], Yongchao Yao[5], Xiang Peng[1]*, Xuping Sun[5,6]*

[1]State Key Laboratory of Green and Efficient Development of Phosphorus Resources, Hubei Key Laboratory of Plasma Chemistry and Advanced Materials, Wuhan Institute of Technology, Wuhan 430205, Hubei, China. [2]School of Textile Science and Engineering, Xi'an Polytechnic University, Xi'an 710048, Shaanxi, China. [3]The State Key Laboratory of Refractories and Metallurgy, Institute of Advanced Materials and Nanotechnology, Wuhan University of Science and Technology, Wuhan 430081, Hubei, China. [4]Department of Physics, Faculty of Science, Islamic University of Madinah, Madinah 42351, Saudi Arabia. [5]Center for High Altitude Medicine, West China Hospital, Sichuan University, Chengdu 610041, Sichuan, China. [6]College of Chemistry, Chemical Engineering and Materials Science, Shandong Normal University, Jinan 250014, Shandong, China.

*Correspondence and requests for materials should be addressed to X.P. (email: xpeng@wit.edu.cn) or X.S. (email: xpsun@uestc.edu.cn)

Abstract

The hydrogen spillover effect offers a promising strategy to overcome the kinetic bottleneck of proton desorption in hydrogen evolution reaction catalysts. However, conventional hydrogen spillover mechanisms rely on interfacial proton transfer between distinct phases and suffer from inherent energy barriers. Here, we show a non-interfacial hydrogen spillover mechanism in a $Ni_{17}W_3$-WO_2 heterostructure, engineered through the synergistic creation of a built-in strain gradient and directional electron transfer. This design spatially confines the complete hydrogen evolution process within the $Ni_{17}W_3$ phase, thereby circumventing cross-phase migration and reshaping the hydrogen adsorption energy landscape. Experimental and theoretical analyses confirm the elimination of interfacial barriers and establishment of an optimized proton-migration route. The resulting catalyst achieves a low overpotential of 21 mV at 10 mA cm^{-2} in 0.5 M H_2SO_4, along with sustained stability (>1500 hours at 500 mA cm^{-2}) and a Faradaic efficiency of 98.6%. This work demonstrates how tailored heterostructures can bypass interfacial bottlenecks, providing guidance for developing efficient non-precious hydrogen spillover catalysts and advancing sustainable hydrogen production.

Introduction

The urgent transition from fossil fuels to sustainable energy systems demands scalable technologies for green hydrogen production, a cornerstone of the future carbon-neutral economy[1-3]. Acidic electrochemical hydrogen evolution reaction (HER), with its rapid kinetics and compatibility with renewable energy sources like wind and solar, stands out as a key solution. In practice, proton exchange membrane (PEM) electrolyzers, leveraging acidic HER technology, are attractive for industrial-scale hydrogen production due to their proton concentration being orders of magnitude higher than that in alkaline/neutral media[4-6]. However, its widespread adoption hinges on replacing expensive Pt-group catalysts with earth-abundant alternatives, which is a challenge exacerbated by the intrinsic trade-off between proton adsorption and desorption in non-noble metal catalysts[7-8]. Such materials readily adsorb protons (Volmer step), but their high hydrogen-binding energy stifles H_2 release (Heyrovsky/Tafel steps), resulting in unsatisfactory activity[9,10].

Recent advances propose hydrogen spillover (H-spillover) as a remedy, where protons adsorbed on active sites migrate to secondary phases for facilitated desorption. For instance, Wei et al. constructed a V_O-rich Pt/TiO_2 heterostructure, where protons adsorbed on Pt sites and then spillover to TiO_2, enhancing desorption kinetics and achieving an overpotential of approximately 60 mV at a current density of 10 mA cm^{-2}, with 24-hour stability[11]. Similarly, Li et al. demonstrated that Fe-doped Ru/CoP heterostructures reduce interfacial electronic barriers, promoting proton transfer and improving HER activity[12]. These cases reveal a fundamental dilemma that conventional H-spillover relies on interfacial proton transfer, which unavoidably introduces electronic barriers that hinder kinetics and structural stress that compromises

durability. However, existing demonstrations of non-interfacial H-spillover, such as in multi-element single-phase structures (e.g., $La_2Sr_2PtO_{7+\delta}$ and high-entropy oxysulfides)[13-14], face inherent limitations. Their reliance on noble-metal dependency or highly complex compositions, coupled with mechanistic ambiguity due to disordered elemental arrangements, hinders the derivation of a general design principle. The rational design of efficient H-spillover pathways requires precise control over the hydrogen adsorption energy landscape across multiple sites. Strain and electronic structure engineering have emerged as powerful levers for such tuning[15]. Tungsten oxides (particularly WO_2) present advantages as heterostructure components due to their structural adaptability and strong propensity for electronic coupling. By constructing an intimate heterointerface, WO_2 can act as a strategic modulator to impose a controllable strain field and drive directional electron transfer to an adjacent active phase[16]. This synergistic modulation is envisioned to create the internal driving force necessary for steering proton migration along a non-interfacial, intra-phase pathway.

Herein, we report a design strategy to bypass interfacial bottlenecks in H-spillover catalysis (Fig. 1). Through *in situ* phase reconstruction, we construct a $Ni_{17}W_3$-WO_2 heterostructure where the WO_2 phase is deliberately employed not as a primary catalytic site, but as an essential engineering component. Its critical function is to induce a built-in strain gradient and facilitate electron transfer within the contiguous $Ni_{17}W_3$ phase. This concerted action collectively reconfigures the local hydrogen adsorption energetics, thereby constructing an efficient, non-interfacial proton spillover channel confined entirely within the $Ni_{17}W_3$ phase. This non-interfacial H-spillover mechanism, validated by a combination of theoretical and experimental analyses, empowers the catalyst with comparable performance, achieving an overpotential of 21

mV at 10 mA cm^{-2} and long-term stability for 1500 hours at an industrial-grade current density of 500 mA cm^{-2}. This work establishes a paradigm of decoupling multi-step reactions within a single phase via interfacial engineering, providing a generalizable platform for the design of advanced electrocatalysts.

Results

Material characterizations and interfacial charge distribution simulation. The $Ni_{17}W_3$-WO_2 heterostructure, comprising WO_2 and $Ni_{17}W_3$ alloy, was synthesized via *in situ* phase reconstruction through annealing of $NiWO_4$ precursor in N_2/H_2 atmosphere (Fig. 2a). Field emission scanning electron microscopy (FE-SEM) characterization reveals the morphological evolution from precursor to final product. The $NiWO_4$ precursor comprises uniform nanoparticles with an average size of 30.3 nm (Supplementary Fig. 1). Following annealing in a N_2/H_2 atmosphere, the nanoparticulate morphology is largely retained, although the average particle size increases to 38.9 nm due to partial agglomeration during the thermal process (Fig. 2b-c and Supplementary Fig. 2). For reference, the individual components were also characterized. Pure WO_2 exhibits a rod-like morphology with distinct surface striations (Supplementary Fig. 3), whereas $Ni_{17}W_3$ forms as irregular, sintered nanoparticles (Supplementary Fig. 4).

The crystal structure was studied by X-ray diffraction (XRD). The XRD pattern of the precursor can be indexed to $NiWO_4$ (JCPDS#15-0755, Supplementary Fig. 5). Additionally, the Raman spectrum for the precursor is consistent with $NiWO_4$[17] (Supplementary Fig. 6). The diffraction peaks (purple line) of the final product using $(NH_4)_6H_2W_{12}O_{40}\cdot xH_2O$ precursor can be ascribed to monoclinic WO_2 (JCPDS#32-1393, Fig. 2d). While using $NiSO_4\cdot 6H_2O$ and $(NH_4)_6H_2W_{12}O_{40}\cdot xH_2O$ as precursors, the diffraction peaks (cyan line) of the final product can be indexed to the face-

centered cubic $Ni_{17}W_3$ (JCPDS#65-4828). The XRD pattern (pink line) of the product obtained by annealing the $NiWO_4$ precursor indicates the formation of a composite of $Ni_{17}W_3$ phase and WO_2 phase.

The high-angle annular dark field scanning transmission electron microscopy (HAADF-STEM) images of $Ni_{17}W_3$-WO_2 reveal that it exhibits a nanoparticle morphology consistent with SEM images (Fig. 2e). The elemental maps indicate the uniform distribution of Ni, W, and O within the $Ni_{17}W_3$-WO_2 (Fig. 2f). The atomic resolution HAADF-STEM image of $Ni_{17}W_3$-WO_2 shows lattice fringes with spacings of d_1=0.35 nm and d_2=0.25 nm, which are attributed to the (011) and (020) planes of the WO_2 phase (Fig. 2g, Supplementary Fig. 7), respectively. The angle between WO_2(011) and WO_2(020) planes is 45°, matching the standard crystal structure of WO_2. While the observed lattice fringe d_3=0.24 nm corresponds to the (111) planes of the $Ni_{17}W_3$ phase (Supplementary Fig. 8). In addition, a distinct interface is observed between $Ni_{17}W_3$(111) and WO_2(011) planes. The crystallographic structure of the heterointerface was unequivocally confirmed by Fast Fourier Transform analysis (Fig. 2h). The distinct diffraction spot pattern can be indexed to the superposition of the [011] zone axis of the face-centered cubic $Ni_{17}W_3$ phase and the [001] zone axis of the monoclinic WO_2 phase. These results provide definitive evidence for the coexistence of $Ni_{17}W_3$ and WO_2, confirming the formation of a well-defined heterointerface between them.

Additionally, geometric phase analysis (GPA) was conducted on the heterointerface area (Fig. 2i). The strain distribution along the *xy* direction reveals distinct strain regions within the $Ni_{17}W_3$ phase but negligible strain variation in the WO_2 phase. The strain distributions along the *xx* and *yy* directions exhibit strain regions consistent with those observed along the *xy* direction

(Supplementary Fig. 9). Quantitative strain analysis along the trajectory in Fig. 2i reveals a pronounced gradient within the $Ni_{17}W_3$ phase, with values ranging from –0.2% to 1.1% and tapering to near zero (–0.05% to 0.03%) at the heterointerface, while the WO_2 phase remains minimally strained (–0.05% to 0, Fig. 2j). This profile signifies a substantial release of intrinsic $Ni_{17}W_3$ lattice stress at the interface, induced by the lattice misfit with WO_2. The well-defined $Ni_{17}W_3$-WO_2 heterointerface-induced strain gradient is posited to establish a continuous modulation of hydrogen adsorption energy across the $Ni_{17}W_3$ phase, thereby facilitating directional proton spillover and enhancing the hydrogen evolution kinetics[18].

Furthermore, the XRD refinement pattern of $Ni_{17}W_3$-WO_2 shows that the molar fractions of $Ni_{17}W_3$ and WO_2 are 17.7% and 82.3%, respectively (Fig. 3a, b). The X-ray photoelectron spectroscopy (XPS) survey spectra show that W elements can be observed in WO_2, $Ni_{17}W_3$, and $Ni_{17}W_3$-WO_2, while Ni is only found in $Ni_{17}W_3$ and $Ni_{17}W_3$-WO_2 (Fig. 3c). As shown in Fig. 3d, the high-resolution XPS Ni-2*p* spectra of $Ni_{17}W_3$ and $Ni_{17}W_3$-WO_2 indicate characteristic peaks at 856.1/874.0 eV and 858.6/876.2 eV correspond to divalent Ni^{2+} and Ni^{3+}, resulting from surface oxidation[19-21]. The peaks at 862.5/880.6 eV are attributed to the satellite peaks[22]. In addition, the peaks at 852.9 and 870.3 eV for $Ni_{17}W_3$-WO_2 are attributed to metallic state Ni^0 [23], which has shifted by 0.2 eV to higher binding energy compared to the pure $Ni_{17}W_3$. The high-resolution XPS W-4*f* spectra of $Ni_{17}W_3$, $Ni_{17}W_3$-WO_2, and WO_2 were analyzed to investigate the chemical states of W (Fig. 3e). The peaks at 31.3 and 33.5 eV correspond to W^0 in the $Ni_{17}W_3$ phase. The peaks at 32.6/34.4 eV are attributed to W^{4+} in the WO_2 phase. Peaks at 35.0/37.3 eV and 35.9/37.9 eV are assigned to W^{5+} and W^{6+} originating from surface oxidation[24-25]. The peak at 40.5 eV corresponds to the W-5*p* orbital. It is worth noting that the binding energies corresponding to W^0 in $Ni_{17}W_3$-

WO_2 are consistent with those in $Ni_{17}W_3$. However, the peaks corresponding to W^{4+} in $Ni_{17}W_3$-WO_2 shifted by 0.2 eV to lower binding energy compared to those in the pure WO_2 phase. The peak shift of Ni^0 and W^{4+} in $Ni_{17}W_3$-WO_2 compared to the pure phases indicates that electron redistribution occurs at the $Ni_{17}W_3$-WO_2 heterointerface. These results confirm the electronic interaction between the metallic Ni and WO_2 at the heterointerface, where electrons transfer from Ni in the $Ni_{17}W_3$ phase to W in the WO_2 phase.

Density functional theory (DFT) calculations were used to further study the charge redistribution of the heterointerface. The work functions of $Ni_{17}W_3$ and WO_2 were calculated independently to clarify the electron transfer path. The work function of pure $Ni_{17}W_3$ is 3.92 eV, while 4.78 eV for pure WO_2 (Fig. 3f, Supplementary Fig. 10). Therefore, electrons will transfer from the $Ni_{17}W_3$ phase to the WO_2 phase at the $Ni_{17}W_3$-WO_2 heterointerface. The electron density difference of the $Ni_{17}W_3$-WO_2 heterointerface reveals that electrons accumulate on the W atoms of the WO_2 phase, while $Ni_{17}W_3$ is electron-depleted (Fig. 3g). Additionally, the Mulliken charge value of W atoms in the WO_2 side at the heterointerface is significantly lower than that at non-interface regions. The opposite trend is observed for the $Ni_{17}W_3$ phase with a higher Mulliken charge value at the heterointerface compared to the non-interface regions (Fig. 3h). These results suggest the presence of electronic interaction at the heterointerface and electrons moving from the $Ni_{17}W_3$ phase to W atoms in the WO_2 phase, which is consistent with the XPS results. The charge redistribution at the heterointerface would alter the hydrogen adsorption properties, thus possibly optimizing the electrocatalytic reaction pathway and enhancing the HER activity[26].

Electrocatalytic HER performance evaluation. The linear sweep voltammetry (LSV) curves of $Ni_{17}W_3$, WO_2, and $Ni_{17}W_3$-WO_2 in 0.5 M H_2SO_4 obtained on glassy carbon (GC) reveal that the

$Ni_{17}W_3$-WO_2 exhibits improved HER activity (Fig. 4a), requiring an overpotential of only 74 ± 3 mV to afford a current density of 10 mA cm^{-2}, which is much lower than that of pure $Ni_{17}W_3$ (232 ± 7 mV) and pure WO_2 (cannot achieve this current density). The corresponding non-*iR* corrected polarization curves are shown in Supplementary Fig. 11. The $Ni_{17}W_3$-WO_2 also demonstrates notable mass activity compared to pure $Ni_{17}W_3$ and WO_2, achieving a mass activity of 0.1 A mg^{-1} at an overpotential of a mere 200 mV (Supplementary Fig. 12). In addition, the Tafel slope of $Ni_{17}W_3$-WO_2 is 48.9 mV dec^{-1} (Fig. 4b), which is smaller than those of pure $Ni_{17}W_3$ (105.0 mV dec^{-1}) and WO_2 (406.6 mV dec^{-1}). This indicates that WO_2 is controlled by the Volmer-step (V-step), and both $Ni_{17}W_3$ and $Ni_{17}W_3$-WO_2 follow the Volmer-Heyrovsky (V-H) reaction mechanism, where the V-step occurs rapidly, and thus the rate-determining step is H-step[27]. Furthermore, the $NiWO_4$ precursor exhibits poor activity in HER, achieving a current density of 1 mA cm^{-2} at an overpotential of 307 ± 9 mV (Supplementary Fig. 13a). It also shows a large Tafel slope of 300.3 mV dec^{-1} (Supplementary Fig. 13b) and a large charge transfer resistance (Supplementary Fig. 13c). The smaller overpotential and Tafel slope of $Ni_{17}W_3$-WO_2 indicate enhanced electrocatalytic activity and accelerated hydrogen evolution kinetics.

HER activity depends on the electrochemically active surface area (ECSA), which can be calculated by the electrical double-layer capacitance (C_{dl}) in the non-Faradic regions based on the cyclic voltammetry (CV) curves (Supplementary Figs. 14 and 15). $Ni_{17}W_3$-WO_2 has an ECSA of 1580 cm^2, which is distinctly larger than those of pure phase $Ni_{17}W_3$ (526 cm) and WO_2 (427 cm). The larger ECSA of $Ni_{17}W_3$-WO_2 is attributed to the increased amount of active sites induced by the heterointerface between $Ni_{17}W_3$ and WO_2 phases to activate the inert atoms. ECSA-normalized activity measurements reveal that the $Ni_{17}W_3$-WO_2 exhibits enhanced intrinsic electrocatalytic

activity compared to the pure $Ni_{17}W_3$ and WO_2 (Fig. 4c). Furthermore, the $Ni_{17}W_3$-WO_2 heterostructure exhibits a markedly higher turnover frequency (TOF) than its individual components at identical overpotentials (Fig. 4d), underscoring its improved intrinsic activity. This enhancement is a direct consequence of the heterointerface, where the synergistic interplay between the induced strain field and interfacial electron redistribution optimizes the hydrogen adsorption energy and collectively lowers the kinetic barrier for the reaction, thereby accelerating the HER.

The $Ni_{17}W_3$-WO_2 was supported on carbon cloth ($Ni_{17}W_3$-WO_2/CC) to assess its potential for industrial implementation in 0.5 M H_2SO_4. The electrode achieves low overpotentials of 21 ± 2, 138 ± 4, and 204 ± 5 mV to reach current densities of 10, 500, and 1000 mA cm^{-2}, respectively, coupled with a Tafel slope of 47.8 mV dec^{-1} (Fig. 4e and Supplementary Fig. 16), indicating both high activity and fast kinetics. The corresponding non-*iR* corrected polarization curves are shown in Supplementary Fig. 17. A comprehensive benchmark against state-of-the-art catalysts, including commercial Pt/C[28], Ru[29], Pt_1/OLC[28], NiRuPt/Activated XC-72[30], Pt@WS_2[31], Pt/NC[32], $CoNiPt_{SA}$@G[33], 2H/1T-WS_2-10[34], hcp-RuCu HUNSs[35], Ru/CNT[36], Ru-Co_2Ni[37], Ru-Cu-MoO_2-48h[38], Ru@V-RuO_2/C HMS[39], Ru-6CDs/G[40], Ru/Pd_2Cu-70[41], Pt_1Ru_1/NMHCS-A[42], $RuSe_2$[43], Ni SA/rGO-CTAB-MoS_2[44], p^+-WS_2-9.8[45], Ni/WC[46], MoS_{2-x}-NbS_x[47], Pb-CoSe2-DETA[48], and $Ni_{0.1}Co_{0.9}Se_2$/NCHP[49] (Supplementary Table 1), reveals that $Ni_{17}W_3$-WO_2/CC is highly competitive with commercial Pt/C and even surpasses many advanced noble-metal-based catalysts. Although its mass activity may trail behind that of ultra-low-loading Pt single-atom catalysts, the entirely earth-abundant composition of $Ni_{17}W_3$-WO_2 guarantees a high cost-to-performance ratio, a paramount advantage for scalable hydrogen production.

The hydrogen production performance of $Ni_{17}W_3$-WO_2/CC was quantified via the water displacement method (Supplementary Fig. 18). At a constant current of −0.1 A, the system generated H_2 at a rate of 1.85 ± 0.02 mmol h^{-1} with a Faradaic efficiency (FE) of 98.65 ± 0.82%, and gas chromatography confirmed the product was 100% pure H_2 (Supplementary Fig. 19a, b). Control experiments on the individual components revealed a critical insight. Both the H_2 evolution rate and FE of $Ni_{17}W_3$-WO_2/CC were nearly identical to those of pure $Ni_{17}W_3$/CC, and both were higher than the values for WO_2/CC (1.82 ± 0.02 mmol h^{-1}, 97.83 ± 0.82%; Supplementary Figs. 20 and 21). This data strongly indicates that the $Ni_{17}W_3$ phase serves as the primary active site for HER, while the slightly lower FE of WO_2 is likely due to partial proton intercalation into its structure, a known phenomenon where some protons are stored rather than converted to H_2[50]. Consequently, the role of the heterointerface is not to generate new active sites on WO_2, but to profoundly enhance the intrinsic activity of the $Ni_{17}W_3$ phase through electronic and strain engineering, as evidenced by the drastically improved overpotential.

Furthermore, the long-term durability of $Ni_{17}W_3$-WO_2/CC was assessed at an industry-relevant current density of 500 mA cm^{-2}. The catalyst exhibited high stability over 1500 hours of continuous operation, with a negligible average potential decay rate of only 28 μV h^{-1} (Fig. 4f and Supplementary Fig. 22). Post-test characterization confirmed robust structural integrity. The persistence of distinct diffraction peaks in XRD and the clearly resolved lattice fringes at the interface in TEM (Supplementary Figs. 23 and 24) collectively demonstrate that the core heterostructure remains intact. XPS analysis indicated slight superficial oxidation of the $Ni_{17}W_3$ phase, evidenced by an increase in high-valent W and Ni species and a corresponding attenuation of the metallic Ni^0 signal (Supplementary Fig. 25), which likely accounts for the minor activity

decay observed during the prolonged test, without compromising the structural integrity of the bulk material. Such performance establishes $Ni_{17}W_3$-WO_2/CC as a stable non-noble catalyst compared to the reported literature under demanding acidic conditions (Supplementary Table 2).

To assess its viability in practical devices, we integrated $Ni_{17}W_3$-WO_2 as a cathode into a PEM electrolyzer. The catalyst formed a homogeneous ink (Supplementary Fig. 26a), enabling its uniform deposition via brush-coating onto carbon paper to form an integrated electrode (Supplementary Fig. 26b), which is a method amenable to industrial scale-up. In a full-cell configuration with an IrO_2 anode (Supplementary Fig. 27), the $Ni_{17}W_3$-WO_2||IrO_2 electrolyzer delivered a low cell voltage of 1.945 V under room temperature (20 °C) (Fig. 4g, corresponding non-*iR* corrected polarization curves are shown in Supplementary Fig. 28) and 1.650 V at 80 °C for 1000 mA cm^{-2} (Supplementary Fig. 29), a performance competitive with the Pt/C||IrO_2 benchmark. The device demonstrated stable operation at room temperature (20 °C) and at 80 °C, sustaining performance over 1000 cycles at high current densities (500 and 1000 mA cm^{-1}) with negligible degradation in the polarization curve (Supplementary Fig. 30). These results underscore the direct practical utility of $Ni_{17}W_3$-WO_2 as a high-performance, non-precious cathode for industrial hydrogen production.

H-spillover mechanism investigation. CV was conducted to study the proton insertion/extraction process of the catalysts during HER in 0.5 M H_2SO_4 (Supplementary Fig. 31). Generally, a more positive proton insertion potential signifies stronger catalyst adsorption, while a more negative proton release potential indicates stronger release capability[51]. The proton insertion potential follows the order: $Ni_{17}W_3$ (0.360 V) > $Ni_{17}W_3$-WO_2 (0.319 V) > WO_2 (0.305 V) vs. RHE (Fig. 5a),

indicating a systematic weakening of hydrogen adsorption strength upon heterostructure formation compared to pristine $Ni_{17}W_3$. More critically, $Ni_{17}W_3$-WO_2 exhibits a more negative proton extraction potential (0.363 V) than $Ni_{17}W_3$ (0.377 V), signaling a significantly reduced energy barrier for hydrogen desorption. Due to the weak hydrogen adsorption property of WO_2, its proton extraction peak could not be detected [52]. This optimized energetics with moderated adsorption coupled with facilitated desorption is the key factor that enhances the HER activity of the $Ni_{17}W_3$-WO_2 heterostructure, aligning well with the proposed non-interfacial H-spillover pathway.

Electrochemical impedance spectroscopy (EIS) provides further mechanistic insights into the HER process. The Nyquist plot for WO_2 shows a dominant Warburg impedance (Fig. 5b), signifying a rate-limiting proton diffusion process due to its poor adsorption capability, which aligns with the CV data[53]. In contrast, both $Ni_{17}W_3$ and $Ni_{17}W_3$-WO_2 display a capacitive arc, characteristic of a surface-controlled reaction involving H* intermediates[54-55]. The smaller charge-transfer resistance of the $Ni_{17}W_3$-WO_2 heterostructure is consistent with its enhanced HER activity. This is corroborated by the Bode plots, where $Ni_{17}W_3$-WO_2 exhibits a lower characteristic frequency (Fig. 5c), indicating a prolonged electron residence time[50, 56]. This finding is consistent with a multi-step reaction pathway, strongly supporting the involvement of an H-spillover process where proton transfer becomes the kinetic bottleneck[57].

To unequivocally establish the H-spillover mechanism, we performed complementary kinetic and chemical probing experiments. The kinetic isotope effect (KIE) was investigated by substituting H_2SO_4/H_2O with D_2SO_4/D_2O. A significant suppression of the current density in the deuterated electrolyte was observed (Fig. 5d), yielding a KIE value > 2.0 across a wide potential

range (Fig. 5e), which is a definitive signature that a proton-transfer step is rate-determining[58]. This kinetic evidence is consistent with a spillover-limited process. In stark contrast, both pure $Ni_{17}W_3$ and WO_2 exhibit KIE values close to 1 (Supplementary Fig. 32), indicating the absence of a proton-transfer-limited mechanism. Furthermore, the Bode plot showed a characteristic frequency shift to lower values in D_2SO_4/D_2O (Fig. 5f), confirming the slower kinetics originated from deuterium's higher mass.

Beyond kinetics, the catalyst's intrinsic ability to dissociate and transport hydrogen atoms was confirmed by the tungsten blue test. When physically mixed with WO_3 and heated in a dilute H_2 atmosphere, $Ni_{17}W_3$-WO_2 induced a rapid color change of WO_3 from yellow to dark blue, signaling the formation of H_xWO_3 (Supplementary Fig. 33a). A control experiment with pure WO_3 showed no change, proving that hydrogen dissociation and spillover originate solely from $Ni_{17}W_3$-WO_2 catalyst (Supplementary Fig. 33b). This provides tangible proof of the catalyst's spillover function, corroborating the electrochemical KIE findings.

In situ Raman spectroscopy was employed to directly visualize the proton transfer pathways, with comparative analysis of WO_2, $Ni_{17}W_3$, and the $Ni_{17}W_3$-WO_2 heterostructure providing critical insights (Supplementary Fig. 34). For pure WO_2, applying a cathodic potential caused the characteristic W-O peak (~860 cm^{-1}) to weaken and shift (Fig. 5g)[59], a definitive sign of H^+ insertion and reduction[50]. This confirms WO_2's inherent capability to act as a proton acceptor in a conventional spillover process. Strikingly, the behavior of the $Ni_{17}W_3$-WO_2 heterostructure is fundamentally different (Fig. 5h). Under cathodic polarization, the W-O bond signal (780 cm^{-1}) remained stable[60], showing no evidence of proton insertion. Instead, we observed the gradual disappearance of interfacial Ni-O bonds (515 cm^{-1} and 603 cm^{-1}) and the concurrent emergence

and intensification of a Ni-H bond (980 cm^{-1})[61]. This provides evidence that hydrogen is exclusively accumulating and reacting within the $Ni_{17}W_3$ phase, while the adjacent WO_2 phase shows limited participation in proton uptake. This contrast is further contextualized by pure $Ni_{17}W_3$ (Fig. 5i), where the Ni-H bond forms at a less negative potential, consistent with its overly strong, performance-limiting hydrogen adsorption.

To evaluate the generality of the strain-gradient design principle beyond the Ni-W composition, we applied the same *in situ* phase reconstruction protocol to synthesize a $Co_{0.87}W_{0.13}$-WO_2 composite (Supplementary Fig. S35). Electrochemical testing confirmed its HER activity (Supplementary Fig. S36a-b). Critically, this distinct material replicates the key mechanistic fingerprints of non-interfacial spillover established above. A pronounced KIE≈2 (Supplementary Fig. 36c-d) confirms a proton-transfer-limited process. Operando Raman spectroscopy (Supplementary Fig. 37) reveals hydrogen accumulation exclusively within the Co-W alloy phase (weakening of Co-O and emergence of Co-H bond) with no proton insertion into WO_2 (stable W-O bond)[60-62]. The replication of these signature features in a chemically distinct system confirms that the non-interfacial spillover mechanism is a direct consequence of the engineered heterointerface, rather than a peculiarity of the Ni-W composition.

Atomic models of the catalysts were constructed and analyzed using DFT calculations to investigate their catalytic mechanisms (Supplementary Figs. 38 and 39). The electronic structures of WO_2, $Ni_{17}W_3$, and the $Ni_{17}W_3$-WO_2 heterostructure were first examined. All models exhibit metallic character with continuous states at the Fermi level (Supplementary Figs. 40 and 41), wherein the heterostructure demonstrates a more uniform charge distribution that facilitates efficient electron transport[63]. The *d*-band center profile of the catalysts shows that $Ni_{17}W_3$ is

closest to the Fermi level at –2.04 eV (Fig. 6a), followed by $Ni_{17}W_3$-WO_2 (–2.17 eV) and WO_2 (–4.19 eV). The results indicate that $Ni_{17}W_3$ has a stronger hydrogen adsorption capability, while WO_2 shows weaker adsorption, which is consistent with the CV results[64-65]. Therefore, the difficulty in hydrogen desorption at $Ni_{17}W_3$ and adsorption at WO_2 leads to a higher overpotential[66]. The $Ni_{17}W_3$-WO_2 presents a balanced hydrogen adsorption behavior compared to the $Ni_{17}W_3$ and WO_2, thereby optimizing the reaction thermodynamics with a lower overpotential.

DFT calculations of the hydrogen adsorption free energy (ΔG_{H^*}) provide insight into the limitations of the individual phases (Fig. 6b-c). For WO_2, the Volmer step presents a prohibitive energy barrier of 1.041 eV, identifying it as the rate-determining step (RDS). This high barrier confirms the fundamental difficulty in initiating the HER on WO_2 due to its weak proton adsorption. Conversely, on $Ni_{17}W_3$, a W site exhibits the most favorable ΔG_{H^*}, enabling efficient proton adsorption. However, the subsequent hydrogen desorption step (H-step) becomes the RDS with a significant barrier of 0.633 eV. Thus, WO_2 and $Ni_{17}W_3$ are intrinsically limited by the initial adsorption and final desorption steps, respectively, which explains their suboptimal HER activities.

Furthermore, we constructed a realistic $Ni_{17}W_3$-WO_2 heterostructure model incorporating the strain gradient mapped by GPA results to precisely evaluate the HER pathway (Fig. 6d-e). The strains at the N1 (N = nickel site) and W1 (W = tungsten site) are 1.2%, the N2 is 0.15%, and the N3, W2, and W3 are −0.05%. The calculations reveal a strategically engineered gradient of hydrogen adsorption free energy (ΔG_{H^*}) across the $Ni_{17}W_3$ phase, with values decreasing from –0.553 eV at the bulk N1 site to –0.199 eV at the interfacial N3 site. This gradient creates a

thermodynamically driven "proton highway" confined entirely within the $Ni_{17}W_3$ phase (N1→N2→N3), where protons spontaneously migrate from strong-adsorption sites to an optimally weak-adsorption site primed for H_2 release. Auxiliary W sites (W1, W2) within the $Ni_{17}W_3$ phase act as efficient proton reservoirs due to their lower ΔG_{H^*}, supplying protons to the adjacent Ni sites via W1→N1 and W2→N3 pathways. Most decisively, the energy barrier for proton transfer from the optimal Ni site (N3) to the adjacent WO_2 phase (W3 site, ΔG_{H^*} = 0.467 eV) is prohibitively high. This starkly demonstrates that cross-interface proton transfer is both thermodynamically and kinetically unfavorable, ruling out conventional interfacial H-spillover. Instead, the reaction follows a non-interfacial mechanism, wherein the entire process from adsorption to diffusion to desorption is completed within the $Ni_{17}W_3$ phase, decisively bypassing the heterointerface.

Thus, a highly efficient non-interfacial H-spillover channel (N1→N2→N3) is established within the $Ni_{17}W_3$ phase of the $Ni_{17}W_3$-WO_2 heterostructure. The synergy of interfacial electron transfer and the strain gradient collectively engineers this pathway, which features a minimized RDS energy barrier of 0.199 eV, which shows a 10% reduction compared to the unstrained model (Supplementary Fig. 42). This work demonstrates a successful design principle: by leveraging synergistic effects to construct an optimal reaction path within one phase and strategically circumvent interfacial bottlenecks, unlocking exceptional catalytic activity.

Discussion

Our study establishes a paradigm shift in H-spillover catalysis by demonstrating a single-phase-confined proton migration mechanism within a $Ni_{17}W_3$-WO_2 heterostructure. Through the synergistic combination of a built-in strain gradient and directional electron transfer, we have

engineered an efficient proton highway entirely within the $Ni_{17}W_3$ phase, thereby circumventing the kinetic bottlenecks associated with conventional interfacial proton transfer. This mechanism empowers the catalyst with comparable performance, achieving an overpotential of 21 mV at 10 mA cm^{-2}, long-term stability for 1500 hours at an industrial-grade current density of 500 mA cm^{-2}, and FE for hydrogen production of 98.6% in 0.5 M H_2SO_4. More broadly, our findings establish a design principle for multi-step electrocatalysis that is possible to bypass inherent interfacial limitations by decoupling and optimizing reaction pathways within a single phase. This strategy opens avenues for the rational design of advanced (electro)catalysts for a wide range of energy conversion reactions, with future work focused on extending this concept to other alloy-oxide systems.

Methods

Synthesis of $Ni_{17}W_3$-WO_2. 4.0 mmol of $NiC_4H_6O_4{\cdot}4H_2O$ (Macklin, 99.9%) and 4.0 mmol of $Na_2WO_4{\cdot}2H_2O$ (Macklin, 99%) were dissolved in 200 mL of deionized water (DW), which was placed in a water bath and heated to 80 °C for 3 hours. The mixture was filtered and washed several times with DW and ethanol (Sinopharm, ≥99.7), followed by drying and further annealing at 600 °C in the air for 1 hour to obtain the $NiWO_4$ precursor. The $Ni_{17}W_3$-WO_2 heterostructure was produced by annealing the $NiWO_4$ precursor at 600 °C in N_2/H_2 (containing 8% H_2) atmosphere for 10 hours with a ramp rate of 5 °C min^{-1}.

Synthesis of WO_2. 1.0 g of $(NH_4)_6H_2W_{12}O_{40}{\cdot}xH_2O$ (Macklin, 99.5%) was spread in a ceramic boat, which was placed in a tube furnace and heated to 700 °C in an air atmosphere for 1 hour with a ramp rate of 5 °C min^{-1}. The product was then annealed at 600 °C in an N_2/H_2 (containing 8% H_2) atmosphere for 2 hours with a ramp rate of 5 °C min^{-1}. The final product was designated as WO_2.

Synthesis of $Ni_{17}W_3$. 0.4 g $NiSO_4 \cdot 6H_2O$ (Macklin, 99.9%) and 0.062 g $(NH_4)_6H_2W_{12}O_{40} \cdot xH_2O$ were dissolved in 3 mL DW, followed by stirring until the mixture was completely dissolved. Then, 15 mL of ethylene glycol was added, and the mixture was stirred for another 20 min. Then, 2 mL of $NH_3 \cdot H_2O$ was added dropwise to the above aqueous solution, which was then irradiated in the microwave reactor at 200 °C for 8 min. The precipitate was washed and centrifuged with DW and ethanol before drying. The product was then annealed in an N_2/H_2 (containing 8% H_2) atmosphere at 750 °C for 2 hours with a heating rate of 5 °C min^{-1} to obtain the $Ni_{17}W_3$ alloy.

Synthesis of $Co_{0.87}W_{0.13}$-WO_2. The $Co_{0.87}W_{0.13}$-WO_2 composite was synthesized via the same *in situ* phase reconstruction method described for $Ni_{17}W_3$-WO_2, with $CoC_4H_6O_4 \cdot 4H_2O$ (Macklin, 99.5%) used as the cobalt precursor in place of $NiC_4H_6O_4 \cdot 4H_2O$.

Characterizations. Scanning electron microscopy (SEM, Hitachi SU3500) and transmission electron microscopy (TEM, Titan G260-300) combined with energy-dispersive X-ray spectroscopy (EDS) were employed to investigate the surface morphology and elemental distribution of the samples. X-ray diffraction (XRD, LabX XRD-6100, Shimadzu), high-resolution transmission electron microscopy (HR-TEM, FEI Tecnai G2 F20), aberration-corrected scanning transmission electron microscopy (AC-STEM, JEM-ARM300F), and Raman spectroscopy (HR RamLab) were utilized to determine the crystalline structure and phase characteristics of the samples. The surface chemistry of the samples was recorded by X-ray photoelectron spectroscopy (XPS, Thermo Scientific K-Alpha, Thermo Fisher) using a monochromatic Al Kα X-ray source. The purity of the gas was determined by means of gas chromatographic (GC, GC-7820) analysis.

Electrochemical measurements. Electrochemical tests were conducted in 0.5 M H_2SO_4 aqueous solution using a CHI 760E workstation and a conventional three-electrode setup. The electrolyte

(0.5 M H_2SO_4) was prepared by diluting concentrated sulfuric acid (XiLONG SCIENTIFIC 98%) with DW, followed by stirring for 30 min. The resulting solution was used immediately after preparation. The Hg/Hg_2Cl_2 reference electrode (CHI150) was calibrated against a fresh commercial one by measuring their stabilized open-circuit potential (OCP) prior to use. The graphite rod served as the counter electrode. The as-prepared electrocatalysts modified glassy carbon electrode (GCE, CHI104, 3 mm in diameter) served as working electrodes to investigate the HER performance in 100 mL 0.5 M H_2SO_4. To prepare the modified GCE, 16 mg of electrocatalyst was dispersed in a mixture of 600 µL of DW and 400 µL of N, N-dimethylformamide by ultrasonication to form an ink. Then, 4 µL (0.004 × 16 =0.064 mg catalyst) of the ink was dropped onto a clean GCE and dried (0.914 mg cm^{-2}). Then, the GCE was covered with a Nafion solution (5 wt%, 5 µL). Linear sweep voltammetry (LSV) was conducted at a scanning rate of 5 mV s^{-1}. Unless otherwise noted, all potentials were compensated for *iR* corrected and converted to the reversible hydrogen electrode (RHE) using the Nernst equation: $E_{RHE} = E_{Hg/Hg2Cl2} + 0.242 + 0.059 \times pH$. The pH was measured to be 0.62 ± 0.03 by a pH meter (FE28, Mettler Toledo). The solution resistance was determined by electrochemical impedance spectroscopy (EIS) performed at an initial potential of −0.22 V *vs.* RHE in the frequency range of 100 kHz to 0.1 Hz. The Tafel slopes were obtained by plotting the overpotentials (η) *vs*. log currents (log $|j|$) derived from the polarization curves. The double-layer capacitance (C_{dl}) was determined from cyclic voltammetry (CV) curves in the non-Faradaic region at scan rates ranging from 1 to 10 mV s^{-1}, which was subsequently used to estimate the electrochemically active surface area (ECSA). By plotting $\Delta j/2$ at OCP against scan rates, C_{dl} is estimated with the slope. Subsequently, ECSA is determined as ECSA = A*C_{dl}/C_s, where A is the geometric area of the

catalyst, and C_s is the specific capacitance (C_s = 0.04 mF cm^{-2}). A Kinetic Isotope Effect (KIE) experiment was performed in 0.5 M D_2SO_4/D_2O electrolyte at a scanning rate of 5 mV s^{-1}. The large current HER properties were obtained using $Ni_{17}W_3$-WO_2 modified carbon cloth ($Ni_{17}W_3$-WO_2/CC) with a mass loading of 0.914 mg cm^{-2} as a working electrode. The stability test was conducted using $Ni_{17}W_3$-WO_2/CC with a constant current density of 500 mA cm^{-2}. The PEM electrolyzer employed 0.5 M H_2SO_4 as the electrolyte at room temperature (20 °C) or 80 °C with a scan rate of 5 mV s^{-1}. The catalyst ink for PEM was prepared by dispersing 10 mg of catalyst (IrO_2, Pt/C, or $Ni_{17}W_3$-WO_2) in 50 mg of Nafion solution (5 wt%) and 100 mg of ethanol. The mixture was ultrasonicated in an ice bath for 60 min to form a homogeneous suspension. The ink was then brush-coated onto carbon paper and dried under ambient conditions. The catalyst loading was determined by weighing the carbon paper before and after coating and was approximately 10 mg cm^{-2}. A proton exchange membrane (Fumasep FS-990-PK) with a thickness of 90 μm and an area of 2 × 2 cm^2 was used as received without pre-treatment. The tungsten blue experiment was performed in a tube furnace at 180 °C for 30 min under a N_2/H_2 mixed atmosphere (8% H_2).

Calculation methods. The DFT calculation was implemented in the Vienna ab initio simulation package (VASP)[67] via the first-principles plane-wave pseudopotential formation and with the generalized gradient approximation (GGA) of Perdew-Burke-Ernzerhof (PBE) function. For the optimization of the structure, a 420.0 eV cutoff energy, 10^{-5} eV energy convergence accuracy, and 0.03 eV Å^{-1} residual force, a 1 × 1 × 1 **k**-mesh is utilized. For the calculation of free energy for adsorbed hydrogen (ΔG_{H^*}), a 450.0 eV cutoff energy, and 0.02 eV Å^{-1} residual force are utilized. Adsorption energy (E_{ads}) was calculated as: $\Delta E = E_{(surface+H)} - E_{(surface)} - 1/2E_{(H2)}$. ΔG_{H^*} could be

calculated as: $\Delta G_{H^*} = \Delta E + \Delta(ZPE) - T\Delta S$, where the ΔS represents the entropy change. $E_{(surface + H)}$ refers to the total energy of the system after a hydrogen atom is adsorbed on the basal plane, while $E_{(surface)}$ represents the energy of the clean surface, and $E_{(H2)}$ corresponds to the total energy of an isolated H_2 molecule. The Δ(ZPE) denotes the zero-point energy (ZPE) difference between an adsorbed hydrogen atom and a gaseous H_2 molecule, as determined through normal mode analysis[68-69]. In this experiment, the entropy of gaseous hydrogen under standard conditions (1 bar of H_2, pH = 0, and temperature T = 298.15 K) was taken into account. The strain model was constructed by stretching (1.2% and 0.15%) and compressing (−0.05%) the crystal structure of the model along the direction parallel to the surface. The corresponding models are included in Supplementary Data 1. It should be noted that while DFT calculations provide valuable insights into the electronic structure, there are inherent limitations in modeling the exact material under actual catalytic conditions.

Data availability. The source data generated in this study are provided in the Source Data file. Source data are provided with this paper.

References

1. Zhang, W. *et al.* Water electrolysis toward elevated temperature: Advances, challenges and frontiers. *Chem. Rev.* **123**, 7119-7192 (2023).
2. Green, F., Bois von Kursk, O., Muttitt, G. & Pye, S. No new fossil fuel projects: The norm we need. *Science* **384**, 954-957 (2024).
3. Sha, Q. *et al.* 10,000-h-stable intermittent alkaline seawater electrolysis. *Nature* **639**, 360-367 (2025).

4. Guan, D. *et al.* Hydrogen society: from present to future. *Energy Environ. Sci.* **16**, 4926-4943 (2023).

5. Glenk, G. & Reichelstein, S. Economics of converting renewable power to hydrogen. *Nat. Energy* **4**, 216-222 (2019).

6. Zhai, W. *et al.* Recent progress on the long-term stability of hydrogen evolution reaction electrocatalysts. *InfoMat* **4**, e12357 (2022).

7. Kosmala, T. *et al.* Operando visualization of the hydrogen evolution reaction with atomic-scale precision at different metal-graphene interfaces. *Nat. Catal.* **4**, 850-859 (2021).

8. Liang, J. *et al.* Electroreduction of alkaline/natural seawater: Self-cleaning Pt/carbon cathode and on-site co-synthesis of H_2 and Mg hydroxide nanoflakes. *Chem* **10**, 3067-3087 (2024).

9. Zuo, Y. *et al.* Ru-Cu nanoheterostructures for efficient hydrogen evolution reaction in alkaline water electrolyzers. *J. Am. Chem. Soc.* **145**, 21419-21431 (2023).

10. Wang, J., Xu, F., Jin, H., Chen, Y. & Wang, Y. Non-noble metal-based carbon composites in hydrogen evolution reaction: Fundamentals to applications. *Adv. Mater.* **29**, 1605838 (2017).

11. Wei, Z.-W. *et al.* Reversed charge transfer and enhanced hydrogen spillover in platinum nanoclusters anchored on titanium oxide with rich oxygen vacancies boost hydrogen evolution reaction. *Angew. Chem. Int. Ed.* **60**, 16622-16627 (2021).

12. Li, J. *et al.* Boosting electrocatalytic activity of Ru for acidic hydrogen evolution through hydrogen spillover strategy. *ACS Energy Lett.* **7**, 1330-1337 (2022).

13. Dai, J. *et al.* Hydrogen spillover in complex oxide multifunctional sites improves acidic hydrogen evolution electrocatalysis. *Nat. Commun.* **13**, 1189 (2022).

14. Jo, S., Shin, K. H., Kim, E. & Sohn, J. I. High-entropy oxychalcogenide for hydrogen spillover enhanced hydrogen evolution reaction in proton and anion exchange membrane water electrolyzers. *Small* **21**, 2411883 (2025).

15. Li, J., Ma, Y., Ho, J. C. & Qu, Y. Hydrogen spillover phenomenon at the interface of metal-supported electrocatalysts for hydrogen evolution. *Acc. Chem. Res.* **57**, 895-904 (2024).

16. Peng, Q. *et al.* Lattice strain induced $Ni_{0.85}Se/WO_{2.90}$ heterostructures accelerate dynamic reconstruction for efficient water oxidation. *Appl. Catal. B-Environ. Energy* **384**, 126158 (2026).

17. Lima, N. A. *et al.* $NiWO_4$ powders prepared via polymeric precursor method for application as ceramic luminescent pigments. *J. Adv. Ceram.* **9**, 55-63 (2020).

18. Borkar, S. S. & Shetty, M. Elucidating the role of strain in catalysis toward modulating surface-adsorbate interactions and tuning catalytic activity. *ChemRxiv* DOI:10.26434/chemrxiv-2024-8ltp5, (2024).

19. Liang, J. *et al.* Efficient bubble/precipitate traffic enables stable seawater reduction electrocatalysis at industrial-level current densities. *Nat. Commun.* **15**, 2950 (2024).

20. Ma, Y. *et al.* High-entropy metal-organic frameworks for highly reversible sodium storage. *Adv. Mater.* **33**, 2101342 (2021).

21. Li, Y. *et al.* Multimetal borides nanochains as efficient electrocatalysts for overall water splitting. *Small* **15**, 1804212 (2019).

22. Hu, W. *et al.* Zirconium doping facilitates a vertically aligned NiCoZr-layered hydroxide nanoneedle arrays electrode for hybrid supercapacitors exhibiting a 90,000 cycle durability. *J. Energy Storage* **97**, 112825 (2024).

23. Zhuo, S. *et al.* Dual-template engineering of triple-layered nanoarray electrode of metal chalcogenides sandwiched with hydrogen-substituted graphdiyne. *Nat. Commun.* **9**, 3132 (2018).

24. Jiang, F. *et al.* A straightforward solvent-pair-enabled multicomponent coassembly approach toward noble-metal-nanoparticle-decorated mesoporous tungsten oxide for trace ammonia sensing. *Adv. Mater.* **36**, 2313547 (2024).

25. Li, J. *et al.* Elucidating the critical role of ruthenium single atom sites in water dissociation and dehydrogenation behaviors for robust hydrazine oxidation-boosted alkaline hydrogen evolution. *Adv. Funct. Mater.* **32**, 2109439 (2022).

26. Li, Y., Hassan, M. S., Zhao, X. & Rogach, A. L. Heterostructured electrocatalysts: from fundamental microkinetic model to electron configuration and interfacial reactive microenvironment. *Adv. Mater.* **37**, 2418146 (2025).

27. Zhao, G., Rui, K., Dou, S. X. & Sun, W. Heterostructures for electrochemical hydrogen evolution reaction: A review. *Adv. Funct. Mater.* **28**, 1803291 (2018).

28. Liu, D. *et al.* Atomically dispersed platinum supported on curved carbon supports for efficient electrocatalytic hydrogen evolution. *Nat. Energy* **4**, 512-518 (2019).

29. Fan, H. *et al.* Revealing the role of Ru-O-Ce interface coupling in CeO_2-Ru aerogel for boosting hydrogen evolution kinetics. *Adv. Energy Mater.* **15**, 2405681 (2025).

30. Huynh, T. T., Mai, V. T. T., Nguyen, A. Q. K. & Pham, H. Q. Ni-doped RuPt nanoalloy on acid-treated carbon for pH-universal hydrogen evolution reaction. *Adv. Sustainable Syst.* **8**, 2300380 (2024).

31. Feng, Y. *et al.* Electronic metal-support interaction induces hydrogen spillover and platinum utilization in hydrogen evolution reaction. *Angew. Chem. Int. Ed.* **64**, e202413417 (2025).

32. Zhang, S.-N. *et al.* Amplifying intermetal bias of Pt-Rh alloy nanolayers for facilitated hydrogen inter-diffusion and evolution. *Angew. Chem. Int. Ed.* **64**, e202512299 (2025).

33. He, H. *et al.* Facile synthesis of high areal density and stable Pt single-atom electrocatalysts by arc discharge atomization and coni trapping. *Adv. Sci.* **12**, e11806 (2025).

34. Siva, P. & Vasu, K. Enhanced hydrogen evolution and symmetric supercapacitor performance of a Ru-doped multiphase WS_2 electrode. *J. Mater. Chem. A* **12**, 961-967 (2024).

35. Zhang, J. *et al.* Face-centered cubic structured RuCu hollow urchin-like nanospheres enable remarkable hydrogen evolution catalysis. *Sci. China Chem.* **65**, 87-95 (2022).

36. Zhang, X. *et al.* Chlorine coordination engineering optimizes hydrogen evolution reaction kinetics on Ru(100) facet. *Adv. Funct. Mater.* **35**, 202508730 (2025).

37. Majumdar, A. *et al.* Strain engineering of Ru-Co_2Ni nanoalloy encapsulated with carbon nanotubes for efficient anion and proton exchange membrane water electrolysis. *Adv. Funct. Mater.* **35**, 2420517 (2025).

38. Liu, Q. *et al.* Nearly hollow Ru-Cu-MoO_2 octahedrons consisting of clusters and nanocrystals for high efficiency hydrogen evolution reaction. *J. Mater. Chem. A* **10**, 12341-12349 (2022).

39. Li, Y. *et al.* Arming Ru with oxygen-vacancy-enriched RuO_2 sub-nanometer skin activates unique bifunctionality for pH-universal overall water splitting. *Adv. Mater.* **35**, 2206351 (2023).

40. Qiang, L. *et al.* Carbon dot-driven spatial and electronic modulation of Ru on graphene for pH-universal hydrogen evolution reaction electrocatalysts. *Green Chem.* **27**, 12364-12377 (2025).

41. Wang, J., Zhang, G., Liu, H., Wang, L. & Li, Z. Ru regulated electronic structure of Pd_xCu_y nanosheets for efficient hydrogen evolution reaction in wide pH range. *Small* **20**, 2310277 (2024).

42. Zhao, W. *et al.* Pt-Ru dimer electrocatalyst with electron redistribution for hydrogen evolution reaction. *ACS Catal.* **12**, 5540-5548 (2022).

43. Zhu, T. *et al.* Amorphous ruthenium-selenium nanoparticles as a pH-universal catalyst for enhanced hydrogen evolution reaction. *ACS Catal.* **14**, 1914-1921 (2024).

44. Liu, H. *et al.* Single-atom nickel encapsulated in nanosheet-coiled rGo-CTAB-MoS_2 nanoflowers for high-efficiency and long-term hydrogen evolution in acidic medium. *Adv. Funct. Mater.* **35**, 2425826 (2025).

45. Siva, P. & Vasu, K. Efficient hydrogen evolution from degenerate-doped *p*-type WS_2 electrocatalysts over a wide pH range. *J. Mater. Chem. A* **12**, 11101-11108 (2024).

46. Ma, Y.-Y. *et al.* Highly efficient hydrogen evolution triggered by a multi-interfacial Ni/WC hybrid electrocatalyst. *Energy Environ. Sci.* **11**, 2114-2123 (2018).

47. Naseem, M. *et al.* Tuning the catalytic activity of MoS_{2-x}-NbS_x heterostructure nanosheets for bifunctional acidic water splitting. *Small* **21**, 2501464 (2025).

48. Wu, R. *et al.* Dopant triggered atomic configuration activates water splitting to hydrogen. *Nat. Commun.* **14**, 2306 (2023).

49. Li, J. *et al.* Hollow bimetallic cobalt-based selenide polyhedrons for efficient hydrogen production in practical PEM electrolysis. *ACS Sustainable Chem. Eng.* **12**, 10020-10032 (2024).

50. Chen, Z. *et al.* Metallic W/WO_2 solid-acid catalyst boosts hydrogen evolution reaction in alkaline electrolyte. *Nat. Commun.* **14**, 5363 (2023).

51. Kwon, J. *et al.* Tailored electronic structure of Ir in high entropy alloy for highly active and durable bifunctional electrocatalyst for water splitting under an acidic environment. *Adv. Mater.* **35**, 2300091 (2023).

52. Chen, J. *et al.* Reversible hydrogen spillover in Ru-WO_{3-x} enhances hydrogen evolution activity in neutral pH water splitting. *Nat. Commun.* **13**, 5382 (2022).

53. Hou, S. *et al.* Ru single atoms tailoring the acidity of metallic tungsten dioxide for a boosted alkaline hydrogen evolution reaction. *ACS Catal.* **14**, 8238-8251 (2024).

54. Zhao, H. *et al.* Raw biomass electroreforming coupled to green hydrogen generation. *Nat. Commun.* **12**, 2008 (2021).

55. Du, H. *et al.* Unlocking interfacial electron transfer of ruthenium phosphides by homologous core-shell design toward efficient hydrogen evolution and oxidation. *Adv. Mater.* **34**, 2204624 (2022).

56. Yan, Y. *et al.* H-buffer effects boosting H-spillover for efficient hydrogen evolution reaction. *Energy Environ. Sci.* **17**, 6024-6033 (2024).

57. Yuan, C. *et al.* $K_xNa_yH_{(2-x-y)}Ti_2O_5$ for high-performance lithium-ion battery anode with Li dendrites-free mechanism, zero-strain characteristic. *Adv. Energy Mater.* **13**, 2302015 (2023).

58. Wang, Q. *et al.* 2D metastable-phase hafnium oxide triggers hydrogen spillover for boosting hydrogen production. *Adv. Mater.* **37**, 2415978 (2025).

59. Bastians, S., Crump, G., Griffith, W. P. & Withnall, R. Raspite and studtite: Raman spectra of two unique minerals. *J. Raman Spectrosc.* **35**, 726-731 (2004).

60. Ross-Medgaarden, E. I. & Wachs, I. E. Structural determination of bulk and surface tungsten oxides with UV-vis diffuse reflectance spectroscopy and Raman spectroscopy. *J. Phys. Chem. C* **111**, 15089-15099 (2007).

61. Guo, P. *et al.* Heterojunction-induced rapid transformation of Ni^{3+}/Ni^{2+} sites which mediates urea oxidation for energy-efficient hydrogen production. *Adv. Mater.* **36**, 2311766 (2024).

62. Wang, Y. *et al.* Defect-induced Zn-Co pair active site for high-efficiency electrosynthesis of H_2O_2. *Matter* **8**, 102479 (2025).

63. You, S. *et al.* Quantifying the conductivity of a single polyene chain by lifting with an STM tip. *Nat. Commun.* **15**, 6475 (2024).

64. Liu, J. *et al.* Optimizing hydrogen adsorption by *d-d* orbital modulation for efficient hydrogen evolution catalysis. *Adv. Energy Mater.* **12**, 2103301 (2022).

65. Wang, J. *et al.* Switch volmer-heyrovsky to volmer-tafel pathway for efficient acidic electrocatalytic hydrogen evolution by correlating Pt single atoms with clusters. *Small* **20**, 2309427 (2024).

66. Jin, J. *et al.* Atomic sulfur filling oxygen vacancies optimizes H absorption and boosts the hydrogen evolution reaction in alkaline media. *Angew. Chem. Int. Ed.* **60**, 14117-14123 (2021).

67. Kresse, G. & Hafner, J. Ab initio molecular dynamics for liquid metals. *Phys. Rev. B* **47**, 558-561 (1993).

68. Noerskov, J. K. *et al.* Trends in the exchange current for hydrogen evolution. *J. Electrochem. Soc.* **152**, J23 (2005).

69. Yang, J. *et al.* Ultrahigh-current-density niobium disulfide catalysts for hydrogen evolution. *Nat. Mater.* **18**, 1309-1314 (2019).

Acknowledgements

This work was financially supported by the National Natural Science Foundation of China (Nos. 52002294 and 22379116), Hubei Provincial Natural Science Foundation of China (No. 2021BAA208), and the Open and Innovation Fund of Hubei Three Gorges Laboratory (No. SC250002). The authors also extend their appreciation to the Deanship of Scientific Research, Islamic University of Madinah, Saudi Arabia, for funding this research work.

Contributions

X.S., X.P., and S.X. designed this research and wrote the manuscript. S.X., H.D., and S.C. performed material synthesis and performance tests. Y.M. conducted theoretical calculations. L.X., B.G., X.Z., and Y.Y. performed material characterizations. I.S. polished the manuscript. X.S. and X.P. supervised the research. All authors contributed to and reviewed the manuscript.

Competing interests statement

The authors declare no competing interests.

Additional information

Correspondence and requests for materials should be addressed to X.S. and X.P.

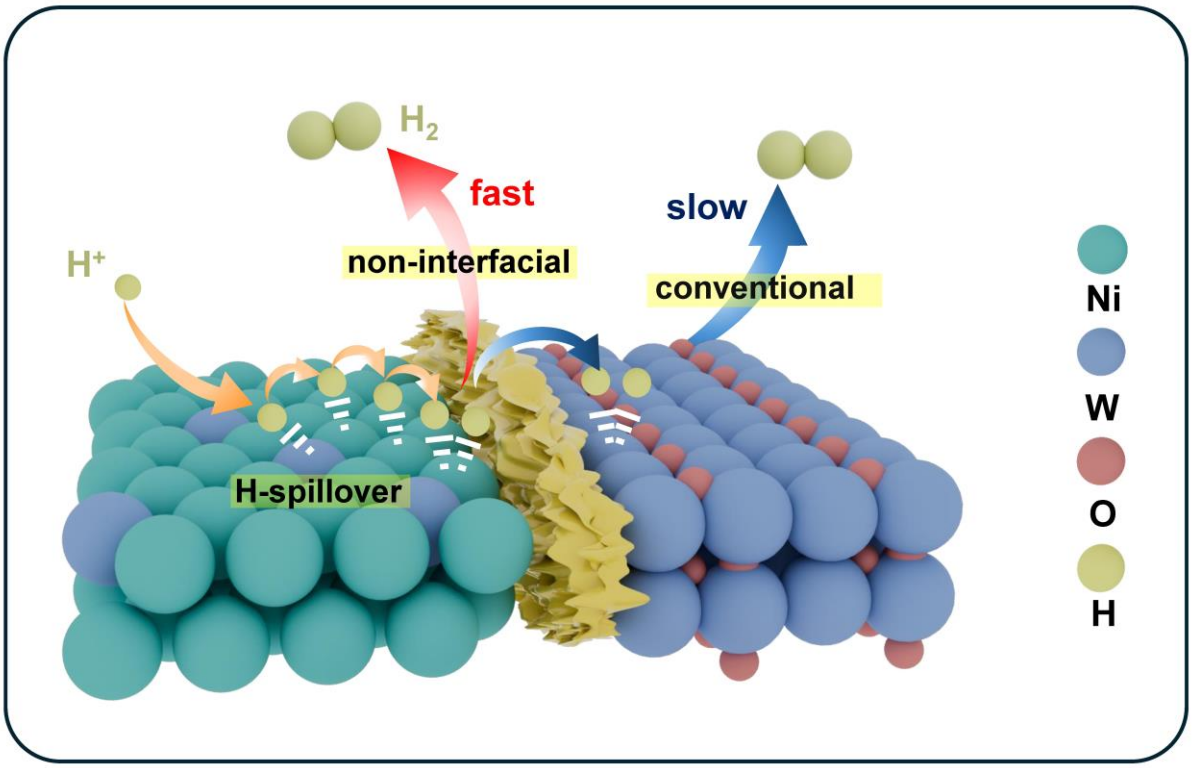

Fig. 1 | Schematic illustration of non-interfacial H-spillover pathway for hydrogen production.

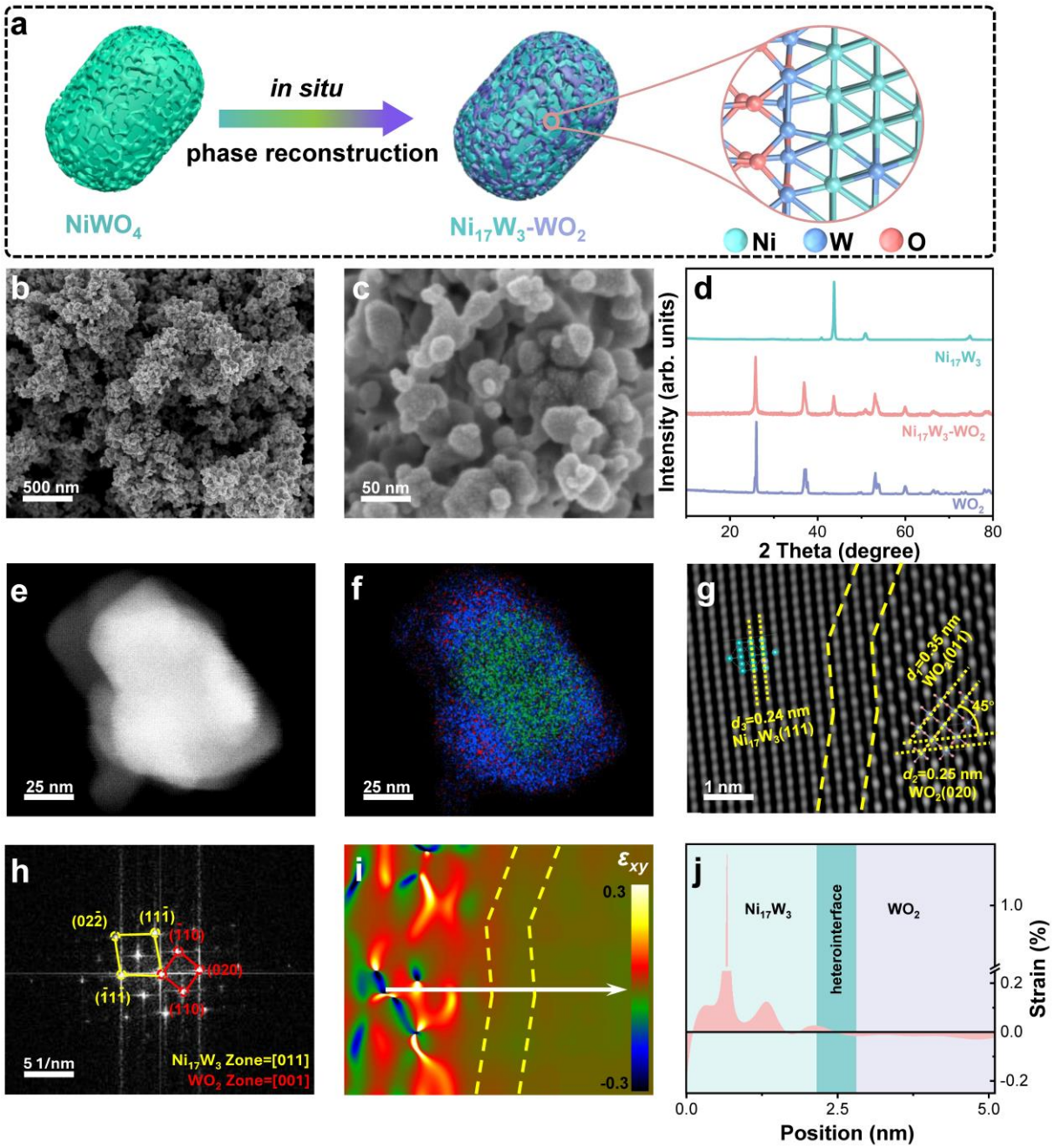

Fig. 2 | Material characterizations. (**a**) Schematic diagram of the construction of $Ni_{17}W_3$-WO_2 heterostructure (Ni, W, and O atoms are shown in cyan, purple, and red, respectively). (**b-c**) FE-SEM images of $Ni_{17}W_3$-WO_2. (**d**) XRD patterns of $Ni_{17}W_3$, WO_2, and $Ni_{17}W_3$-WO_2. (**e**) HAADF-STEM image, (**f**) elemental maps (Ni, W, and O elements are shown in green, blue, and red, respectively), (**g**) atomic resolution HAADF-STEM image, and (**h**) SAED pattern of $Ni_{17}W_3$-WO_2. (**i**) GPA for the

lattice strain maps alone with the *xy* direction. (**j**) Strain profiles taken alone with the white arrow.

Source data are provided as a Source Data file.

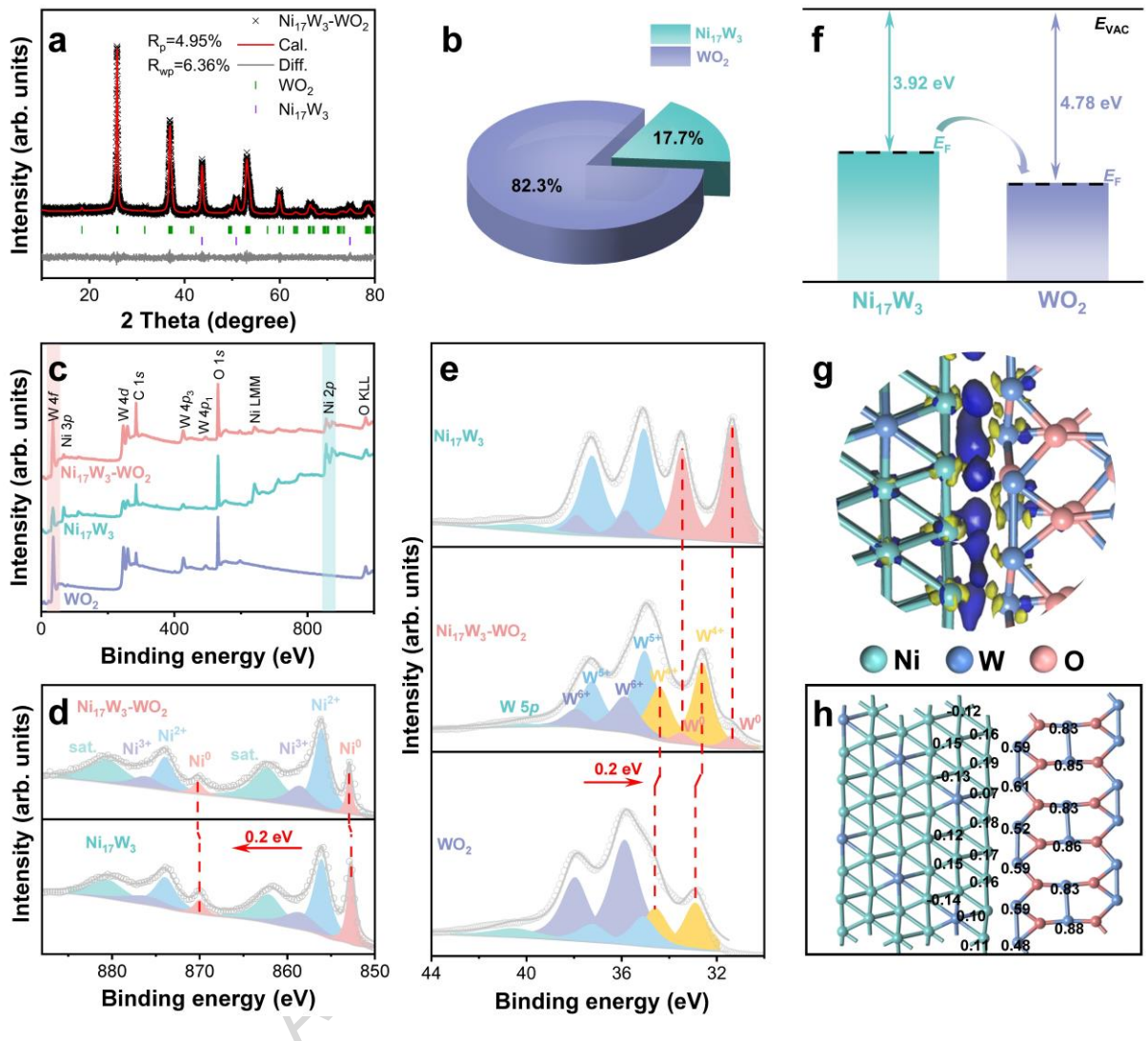

Fig. 3 | Investigation of composition, chemical state, and charge distribution of heterointerface. (**a**) XRD refinement pattern of $Ni_{17}W_3$-WO_2. (**b**) Molar ratio of $Ni_{17}W_3$ and WO_2 phases in $Ni_{17}W_3$-WO_2. (**c**) XPS survey spectra. (**d**) High-resolution XPS Ni-2*p* spectra of $Ni_{17}W_3$-WO_2 and $Ni_{17}W_3$. (**e**) High-resolution XPS W-4*f* spectra of $Ni_{17}W_3$, $Ni_{17}W_3$-WO_2, and WO_2. (**f**) Work functions of $Ni_{17}W_3$ and WO_2. (**g**) Electron density difference of $Ni_{17}W_3$-WO_2 (Ni, W, and O atoms are shown in cyan, purple, and red, respectively) with blue and yellow regions indicating charge accumulation and depletion, respectively. (**h**) Mulliken charge analysis of $Ni_{17}W_3$-WO_2 (Ni, W, and O atoms are shown in cyan, purple, and red, respectively). Source data are provided as a Source Data file.

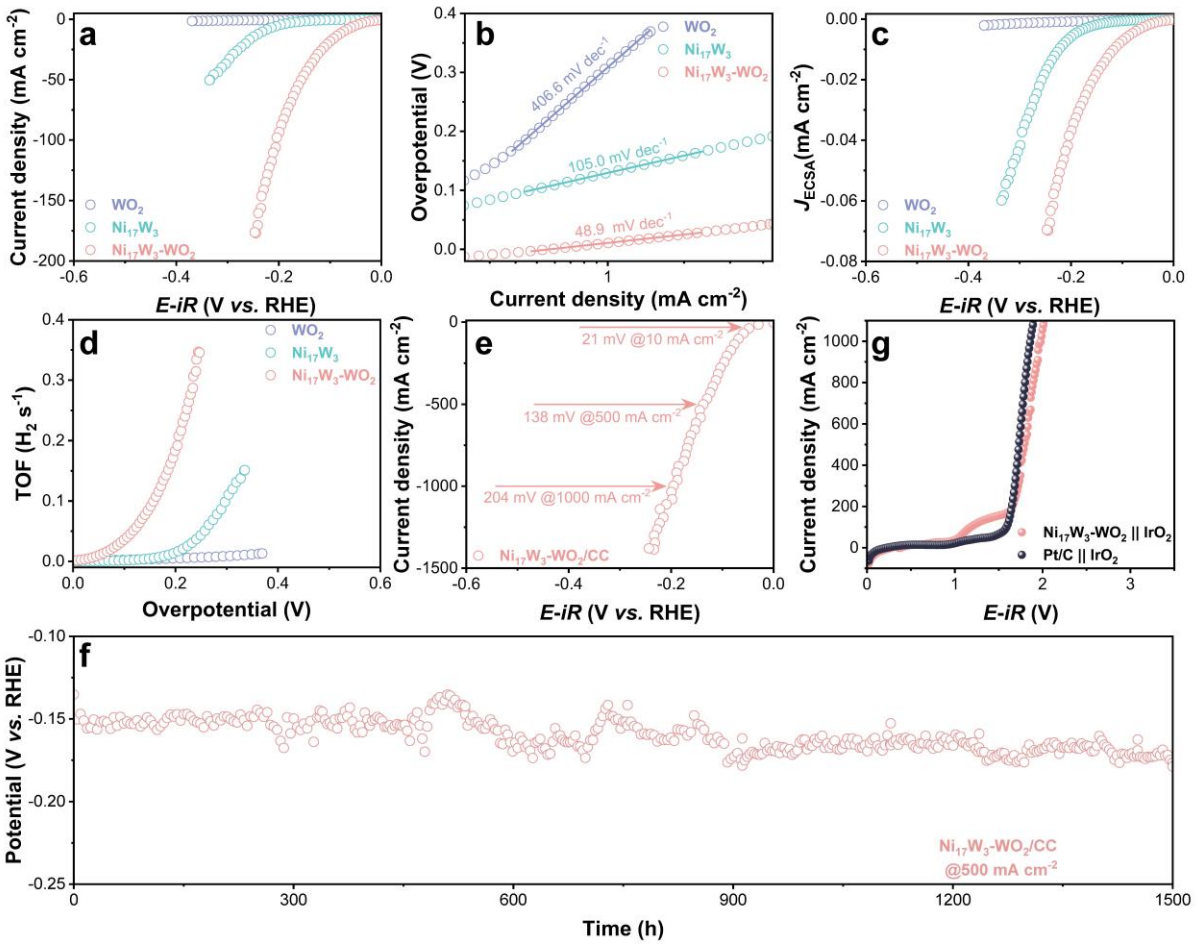

Fig. 4 | Electrocatalytic HER performance evaluation. (**a**) LSV curves with 80% *iR* correction (electrode surface area of 0.0706 cm^2, *R*=12.37 ± 0.3), (**b**) Tafel plots, (**c**) ECSA-normalized LSV curves, and (**d**) TOF of the electrocatalysts on GCE. (**e**) LSV curve of $Ni_{17}W_3$-WO_2/CC with 80% *iR* correction (electrode surface area of 0.70 cm^2, *R*=1.65 ± 0.1). (**f**) Stability test of $Ni_{17}W_3$-WO_2/CC. (**g**) LSV curves of PEM electrolyzers assembled with $Ni_{17}W_3$-WO_2||IrO_2 and Pt/C||IrO_2 configurations at room temperature (20 °C) with 80% *iR* correction (electrode surface area of 0.81 cm^2, *R*=0.5 ± 0.1). All tests were performed in 0.5 M H_2SO_4 (pH=0.62) at a scanning rate of 5 mV s^{-1}. Source data are provided as a Source Data file.

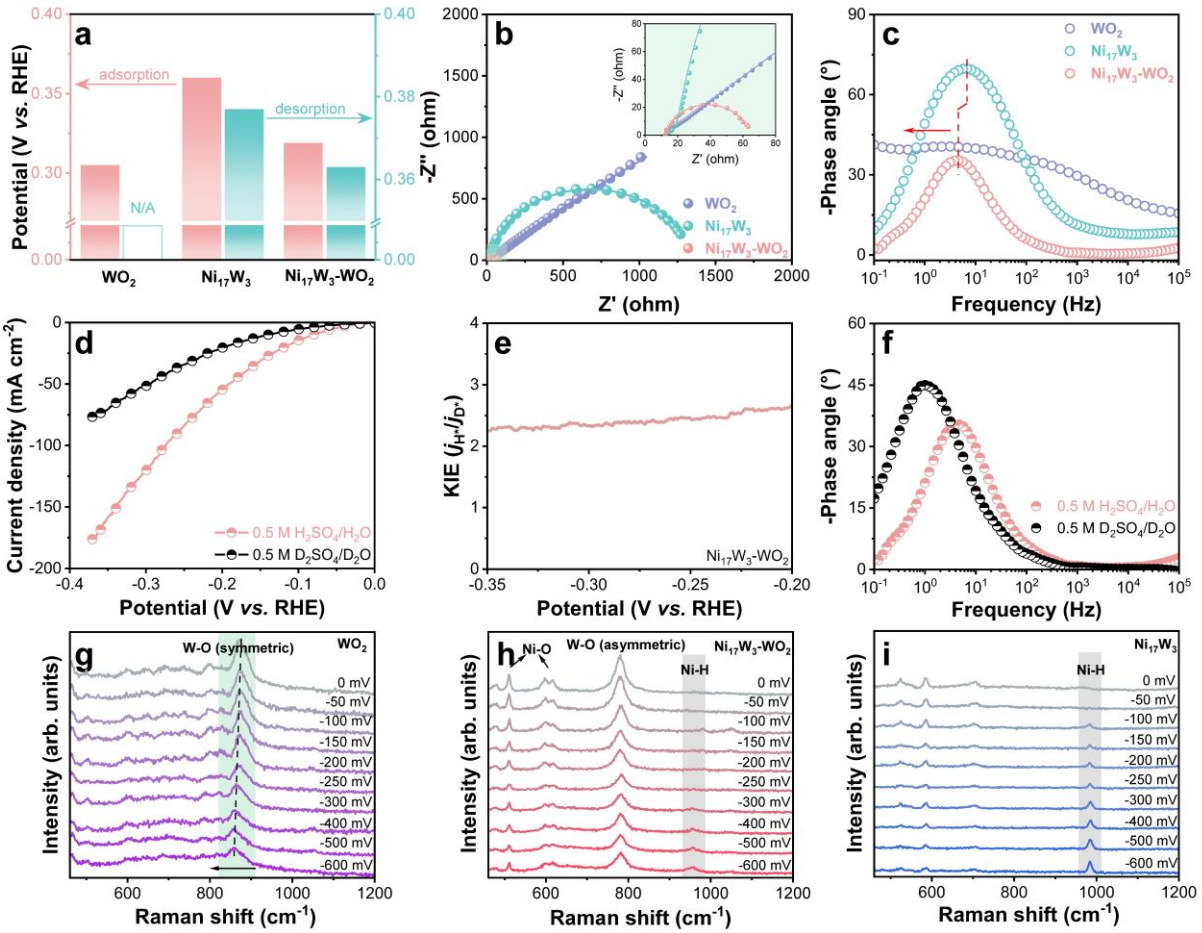

Fig. 5 | Investigation of hydrogen adsorption and desorption properties. (**a**) Adsorption and desorption peak potentials of WO_2, $Ni_{17}W_3$, and $Ni_{17}W_3$-WO_2. (**b**) Nyquist plots with the magnified view shown in the inset and (**c**) Bode plots of WO_2, $Ni_{17}W_3$, and $Ni_{17}W_3$-WO_2. (**d**) Polarization curves of $Ni_{17}W_3$-WO_2 in 0.5 M H_2SO_4 and 0.5 M D_2SO_4 solutions without *iR* correction. (**e**) The KIE value versus potential. (**f**) Bode plots of $Ni_{17}W_3$-WO_2 in 0.5 M H_2SO_4 and 0.5 M D_2SO_4 solutions. *In situ* Raman spectra of (**g**) WO_2, (**h**) $Ni_{17}W_3$-WO_2, and (**i**) $Ni_{17}W_3$ recorded in 0.5 M H_2SO_4 from 0 to −600 mV *vs*. RHE. Source data are provided as a Source Data file.

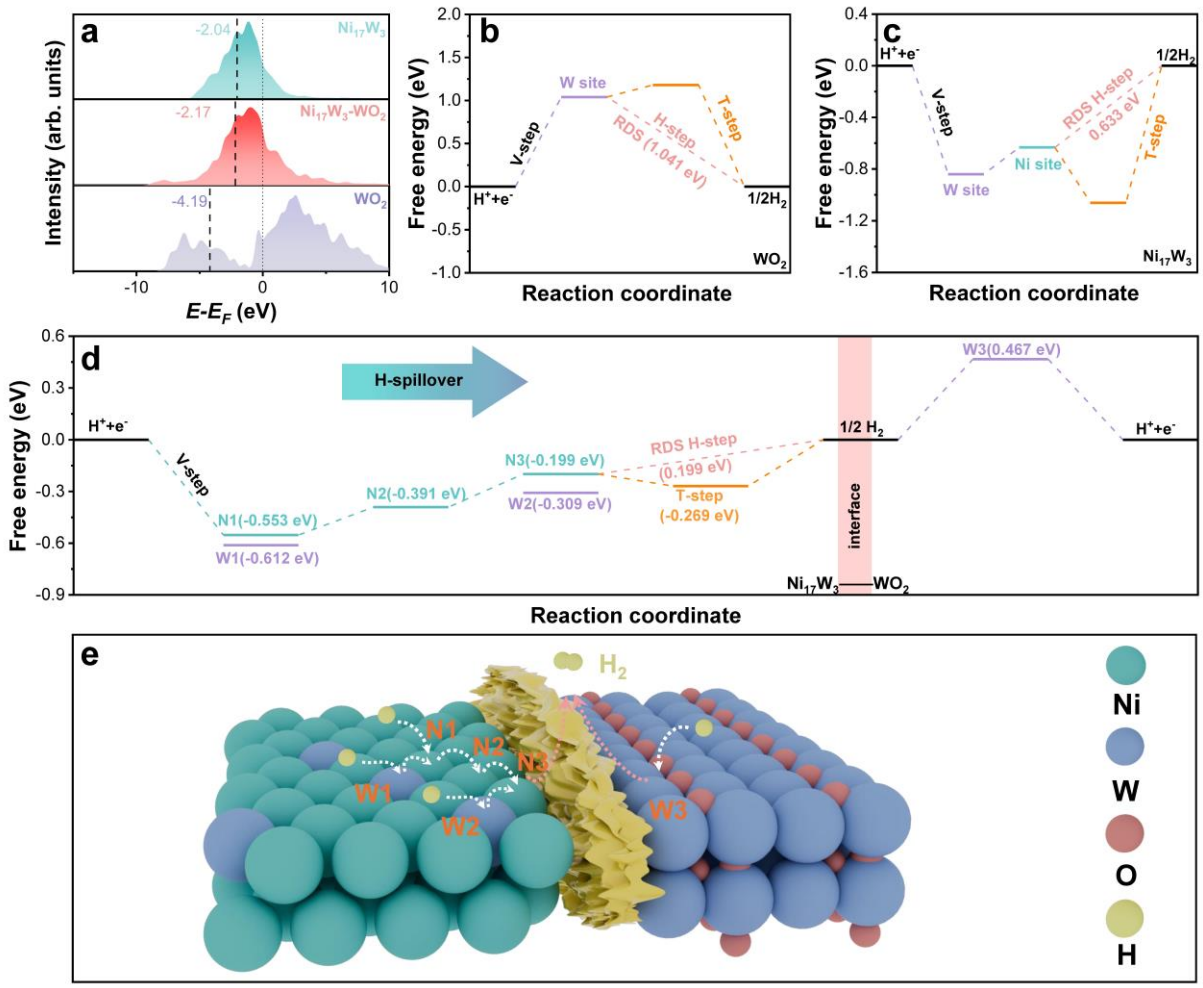

Fig. 6 | Exploring H-spillover mechanism. (**a**) *d*-band centers of $Ni_{17}W_3$, WO_2, and $Ni_{17}W_3$-WO_2. Calculated free energy diagram for HER on (**b**) WO_2, (**c**) $Ni_{17}W_3$, and (**d**) $Ni_{17}W_3$-WO_2. (**e**) The H* adsorption models on various sites of $Ni_{17}W_3$-WO_2. Source data are provided as a Source Data file.

Editor's Summary:

Hydrogen spillover enhances hydrogen production but is hindered by electronic barriers at phase interfaces. Here, the authors report a Ni17W3–WO2 with a built-in strain gradient and directional electron transfer to enable non-interfacial hydrogen spillover, delivering high activity and durability.

Peer review information: *Nature Communications* thanks Huilong Fei, Hyuksu Han and the other anonymous reviewer(s) for their contribution to the peer review of this work. A peer review file is available.